Posterior Cramér-Rao Bounds for Near-Field Radio SLAM

Wankyu Choe, Hyunwoo Park, Kyeongju Cha, and Sunwoo Kim
Department of Electronic Engineering, Hanyang University
{choewg, stark95, lovelyckj, remero}@hanyang.ac.kr

Abstract

In 6G communications, the near-field region is expected to expand further, driven by the significant increase in carrier frequency and the number of antenna elements. Leveraging the spherical wave characteristics inherent to the near-field enables the acquisition of additional information. In this paper, we investigate the benefits of considering the near-field in radio simultaneous localization and mapping (SLAM) by deriving the posterior Cramér-Rao bounds (PCRBs). The theoretical analysis based on the PCRB corroborates the effectiveness of incorporating the near-field measurement in enhancing radio SLAM performance.

***Index Terms*—Near-field, radio SLAM, posterior Cramér-Rao bounds**

I. Introduction

In the next generation of communications, the substantial increase in carrier frequency and antenna array aperture is anticipated to bring about the expansion of the near-field region [1]. The prior work [2] emphasized the efficacy of the involvement of an additional measurement in radio SLAM. This paper studies the benefits of exploiting the near-field measurement in radio SLAM, leveraging the curvature of the spherical wavefronts to estimate scatterer distances from the transmitter or receiver, hereinafter referred to as *near-field distance*. To quantify the additional information and analyze the effect of the measurement quality, the posterior Cramér-Rao bound (PCRB)-based error bounds (EBs) are derived.

II. System Model

The propagation environment consists of a direct path from the base station (BS), reflected paths from the reflecting surfaces, modeled as virtual anchors (VAs), and scattering reflected paths characterized by scattering points (SPs). $\mathbf{x} = \left[\mathbf{x}_{\text{LM}}^{\mathsf{T}}, m\right]^{\mathsf{T}}$ denotes the landmark state, where $\mathbf{x}_{\text{LM}} = [x_{\text{LM}}, y_{\text{LM}}, z_{\text{LM}}]^{\mathsf{T}}$ is location for a landmark type $m \in \mathcal{M}$ with the landmark type set $\mathcal{M} = \{\text{BS, VA, SP}\}$. The BS location $\mathbf{x}_{\text{BS}}$ is known and fixed. The environment is modeled by the landmark set $\mathcal{X} = \{\mathbf{x}^1, \ldots, \mathbf{x}^I\}$ where I is the total number of landmarks.

Vehicle state at time k is denoted by $\boldsymbol{s}_k = \left[\mathbf{v}_k^{\mathsf{T}}, \alpha_k, \zeta_k, \rho_k, B_k\right]^{\mathsf{T}}$, where $\mathbf{v}_k = [x_k, y_k, z_k]^{\mathsf{T}}, \alpha_k, \zeta_k, \rho_k$, and B_k are the position, heading, translation speed, turn-rate, and clock bias, respectively. The vehicle transition density is as follows.

$$f(\boldsymbol{s}_k|\boldsymbol{s}_{k-1}) = \mathcal{N}(\boldsymbol{s}_k; \boldsymbol{v}(\boldsymbol{s}_{k-1}), \boldsymbol{Q}), \tag{1}$$

where $\boldsymbol{v}(\cdot)$ is a known transition function and the process noise covariance $\boldsymbol{Q}$.

In this work, we assume the BS with a single antenna and the vehicle with N-element antenna arrays. At time k, a set of measurements $\mathcal{Z}_k = \{\boldsymbol{z}_k^1, \ldots, \boldsymbol{z}_k^{\hat{I}_k}\}$ is provided through the channel estimation at the receiver, where $\hat{I}_k$ is the number of measurements involving misdetected measurements and clutter measurements at time k. Each elements of the measurement set $\mathcal{Z}_k$ can be expressed as

$$\boldsymbol{z}_k^i = \boldsymbol{h}(\mathbf{x}^i, \boldsymbol{s}_k) + \mathbf{w}_k^i, \tag{2}$$

where $\boldsymbol{h}(\mathbf{x}^i, \boldsymbol{s}_k) = \left[\tau_k^i, (\boldsymbol{\theta}_k^i)^{\mathsf{T}}, d_k^i\right]^{\mathsf{T}}$ and $\mathbf{w}_k^i = \mathcal{N}(\mathbf{w}_k^i; \mathbf{0}, \boldsymbol{\Sigma}_k^i)$ with a known covariance $\boldsymbol{\Sigma}_k^i$. The ToA and near-field distance can be measured as

$$\tau_k^i = \begin{cases} \|\mathbf{v}_k - \mathbf{x}_{\text{LM}}^i\| + B_k & m^i = \text{BS}, \\ \|\mathbf{v}_k - \mathbf{x}_{\text{LM}}^i\| + \|\mathbf{x}_{\text{BS}} - \mathbf{x}_{\text{LM}}^i\| + B_k & m^i \in \{\text{VA, SP}\}, \end{cases} \tag{3}$$

$$d_k^i = \|\mathbf{v}_k - \mathbf{x}_{\text{LM}}^i\| + B_k \quad \forall m^i, \tag{4}$$

where $\mathbf{x}_{\text{LM}}^i$ denotes the landmark location associated with the i-th path, and m^i indicates its type. The detailed formulations for the AoA in azimuth and elevation are described in [3, Appendix B].

III. Fundamental Performance Analysis

The EBs can be obtained by recursively updating a posterior information matrix (PIM) utilizing complete states [4]. A complete state of the system can be expressed as $\check{\boldsymbol{s}}_k = \left[(\boldsymbol{s}_k)^{\mathsf{T}}, (\mathbf{x}_{\text{LM}}^1)^{\mathsf{T}}, \ldots, (\mathbf{x}_{\text{LM}}^I)^{\mathsf{T}}\right]^{\mathsf{T}}$, the transition function of the complete state is denoted as $\check{\boldsymbol{v}}(\check{\boldsymbol{s}}_k) = \left[(\boldsymbol{v}(\boldsymbol{s}_k))^{\mathsf{T}}, (\mathbf{x}_{\text{LM}}^1)^{\mathsf{T}}, \ldots, (\mathbf{x}_{\text{LM}}^I)^{\mathsf{T}}\right]^{\mathsf{T}}$, and the measurement function of the complete state given the true DA is denoted as $\check{\boldsymbol{h}}(\check{\boldsymbol{s}}_k) = \left[(\bar{\boldsymbol{h}}(\mathbf{x}^1, \boldsymbol{s}_k))^{\mathsf{T}}, \ldots, (\bar{\boldsymbol{h}}(\mathbf{x}^I, \boldsymbol{s}_k))^{\mathsf{T}}\right]^{\mathsf{T}}$, where

$$\bar{\boldsymbol{h}}(\mathbf{x}^i, \boldsymbol{s}_k) = \begin{cases} \boldsymbol{h}(\mathbf{x}^i, \boldsymbol{s}_k) & \text{if } i\text{-th landmark is detected}, \\ \mathbf{0}_{d_{\boldsymbol{z}} \times 1} & \text{otherwise}. \end{cases} \tag{5}$$

Suppose $\check{\boldsymbol{H}}_k$ and $\check{\boldsymbol{V}}_k$ represent the Jacobian matrices of $\check{\boldsymbol{h}}(\check{\boldsymbol{s}}_k)$ and $\check{\boldsymbol{v}}(\check{\boldsymbol{s}}_k)$ with respect to $\check{\boldsymbol{s}}_k$, and $\check{\boldsymbol{Q}}_k = \text{blkdiag}(\boldsymbol{Q}, \mathbf{0}_{3I \times 3I})$ and $\check{\boldsymbol{\Sigma}}_k = \text{blkdiag}(\boldsymbol{\Sigma}_k^1, \cdots, \boldsymbol{\Sigma}_k^I)$ denote the complete form of process and measurement noise covariances, respectively. The PIM can be described as a recursive formulation,

$$\boldsymbol{J}_k = \check{\boldsymbol{H}}_k^{\mathsf{T}} \check{\boldsymbol{\Sigma}}_k^{-1} \check{\boldsymbol{H}}_k + (\check{\boldsymbol{Q}}_k + \check{\boldsymbol{V}}_k \boldsymbol{J}_{k-1}^{-1} \check{\boldsymbol{V}}_k^{\mathsf{T}})^{-1}. \tag{6}$$

The positioning EB (PEB), heading EB (HEB), and clock bias EB (CEB) of the vehicle at time k can be computed as

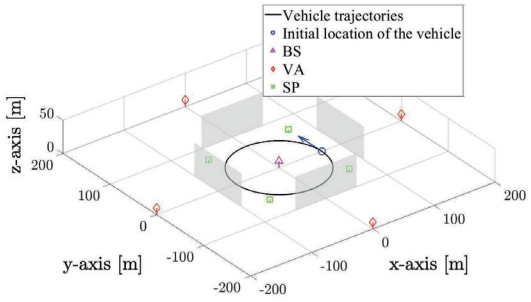

Fig. 1: Vehicle trajectories and map of the simulation environment with 1 BS, 4 VAs, and 4 SPs.

$\sqrt{\sum_{\mu=1}^{3}[\boldsymbol{J}_k]^{-1}_{\mu,\mu}}$, $\sqrt{[\boldsymbol{J}_k]^{-1}_{4,4}}$, and $\sqrt{[\boldsymbol{J}_k]^{-1}_{7,7}}$, respectively, and the landmark EB (LEB) of i-th landmark at time k can be computed as $\sqrt{\sum_{\mu=3i+5}^{3i+7}[\boldsymbol{J}_k]^{-1}_{\mu,\mu}}$.

The first term in (6) represents the information from the measurements at time k, denoted as $\boldsymbol{J}_{\mathrm{D},k}$, and the second term represents the prior information matrix at time k, denoted as $\boldsymbol{J}_{\mathrm{P},k}$. The near-field distance only contributes to $\boldsymbol{J}_{\mathrm{D},k}$, and it can be expressed as two diagonal blocks related to the vehicle state and i-th landmark, respectively,

$$[\boldsymbol{J}_{\mathrm{D},k}]_{1:7,1:7} = \sum_{i=1}^{I}\Big(\frac{\partial\hat{\boldsymbol{h}}(\mathbf{x}^i,\boldsymbol{s}_k)}{\partial\boldsymbol{s}_k}\Big)^{\mathsf{T}}(\hat{\boldsymbol{\Sigma}}_k^i)^{-1}\Big(\frac{\partial\hat{\boldsymbol{h}}(\mathbf{x}^i,\boldsymbol{s}_k)}{\partial\boldsymbol{s}_k}\Big) + \sum_{i=1}^{I}\Big(\frac{\partial d_k^i}{\partial\boldsymbol{s}_k}\Big)^{\mathsf{T}}(\sigma_{d,k}^i)^{-2}\Big(\frac{\partial d_k^i}{\partial\boldsymbol{s}_k}\Big), \tag{7}$$

$$[\boldsymbol{J}_{\mathrm{D},k}]_{3i+5:3i+7,3i+5:3i+7} = \Big(\frac{\partial\hat{\boldsymbol{h}}(\mathbf{x}^i,\boldsymbol{s}_k)}{\partial\mathbf{x}_{\mathrm{LM}}^i}\Big)^{\mathsf{T}}(\hat{\boldsymbol{\Sigma}}_k^i)^{-1}\Big(\frac{\partial\hat{\boldsymbol{h}}(\mathbf{x}^i,\boldsymbol{s}_k)}{\partial\mathbf{x}_{\mathrm{LM}}^i}\Big) + \Big(\frac{\partial d_k^i}{\partial\mathbf{x}_{\mathrm{LM}}^i}\Big)^{\mathsf{T}}(\sigma_{d,k}^i)^{-2}\Big(\frac{\partial d_k^i}{\partial\mathbf{x}_{\mathrm{LM}}^i}\Big), \tag{8}$$

where $\hat{\boldsymbol{h}}(\mathbf{x}^i,\boldsymbol{s}_k) = \big[\bar{\boldsymbol{h}}(\mathbf{x}^i,\boldsymbol{s}_k)\big]_{1:3}$, $\hat{\boldsymbol{\Sigma}}_k^i = \big[\boldsymbol{\Sigma}_k^i\big]_{1:3,1:3}$, and $\sigma_{d,k}^i$ is the standard deviation of the near-field distance measurement noise. The second terms in both (7) and (8) contain non-negative information of both vehicle state and landmarks, which can improve the accuracy of the mapping and vehicle state estimation.

IV. Results

We consider 3D vehicular networks with a single BS, four flat walls, and four SPs, as shown in Fig. 1. The vehicle is moving on a circular road around the BS according to the dynamics (1), with the transition function $\boldsymbol{v}(\cdot)$ [3, Sec. VI] and the process noise modeled as additive zero-mean Gaussian, where its covariance is $\boldsymbol{Q} = \mathrm{diag}[0.04\,\mathrm{m}^2, 0.04\,\mathrm{m}^2, 0, 10^{-6}\,\mathrm{rad}^2, 0, 0, 0.04\,\mathrm{m}^2]$. The measurement noise covariance is set to $\boldsymbol{\Sigma}_k^i = \mathrm{diag}[0.04\,\mathrm{m}^2, 4\times10^{-4}\,\mathrm{rad}^2, 4\times10^{-4}\,\mathrm{rad}^2, \sigma_d^2]$. The BS is located at $[0\,\mathrm{m}, 0\,\mathrm{m}, 10\,\mathrm{m}]^{\mathsf{T}}$, four VAs are located at $[\pm200\,\mathrm{m}, 0\,\mathrm{m}, 10\,\mathrm{m}]^{\mathsf{T}}$ and $[0\,\mathrm{m}, \pm200\,\mathrm{m}, 10\,\mathrm{m}]^{\mathsf{T}}$, and four SPs are located at $[\pm65\,\mathrm{m}, 65\,\mathrm{m}, 5\,\mathrm{m}]^{\mathsf{T}}$ and $[\pm65\,\mathrm{m}, -65\,\mathrm{m}, 5\,\mathrm{m}]^{\mathsf{T}}$. The additional settings and descriptions for the other parameters are provided in [3].

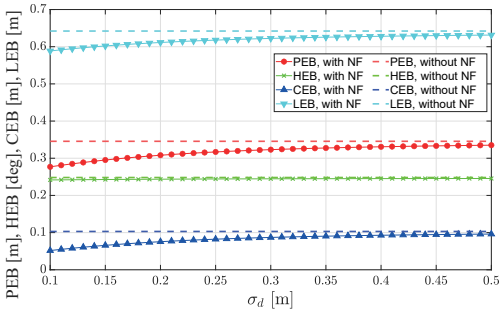

Fig. 2: The PEB, HEB, CEB, and average LEB along σ_d from 0.1 to 0.5, compared with the corresponding lower bounds without exploiting near-field distance.

To demonstrate the contribution of exploiting the near-field distance, we derived the PCRB in Section III. The EBs along the different values of σ_d can be computed based on the PCRB, as shown in Fig. 2. The EBs of the case, considering the near-field distance, are always lower than the EBs without the near-field, where the predefined ranges of σ_d are from 0.1 to 0.5.

V. Conclusion

In this paper, we proposed the near-field radio SLAM framework leveraging the curvature of the spherical wavefronts and analyzed how the near-field distance benefits. The fundamental performance analysis indicated that incorporating the near-field distance into radio SLAM improves the performance for both vehicle state estimation and mapping. Furthermore, we observe that the more accurate estimation of the near-field distance leads to more significant improvements. The results present new opportunities for enhanced radio SLAM by exploiting new measurements, which can be acquired in future communications.

Acknowledgment

This work was supported by the National Research Foundation of Korea(NRF) grant funded by the Korea government(MSIT) (No. NRF-2023R1A2C3002890).

References

[1] M. Cui, Z. Wu, Y. Lu, X. Wei, and L. Dai, "Near-field MIMO communications for 6G: Fundamentals, challenges, potentials, and future directions," *IEEE Communications Magazine*, vol. 61, no. 1, pp. 40–46, 2023.

[2] Y. Ge, O. Kaltiokallio, H. Chen, F. Jiang, J. Talvitie, M. Valkama, L. Svensson, and H. Wymeersch, "Doppler exploitation in bistatic mmWave radio SLAM," in *GLOBECOM 2022 - 2022 IEEE Global Communications Conference*, 2022, pp. 6463–6468.

[3] H. Kim, K. Granström, L. Gao, G. Battistelli, S. Kim, and H. Wymeersch, "5G mmWave cooperative positioning and mapping using multi-model PHD filter and map fusion," *IEEE Transactions on Wireless Communications*, vol. 19, no. 6, pp. 3782–3795, 2020.

[4] P. Tichavsky, C. Muravchik, and A. Nehorai, "Posterior Cramer-Rao bounds for discrete-time nonlinear filtering," *IEEE Transactions on Signal Processing*, vol. 46, no. 5, pp. 1386–1396, 1998.